Meteorol Atmos Phys (2014) 123:1–15
DOI 10.1007/s00703-013-0292-2

ORIGINAL PAPER

Observations of the marine boundary layer under a cutoff low over the southeast Pacific Ocean

David A. Rahn

Received: 30 May 2013 / Accepted: 5 October 2013 / Published online: 16 October 2013

Abstract Stratocumulus is often present offshore of Peru and northern Chile and exists at the top of a cool, moist and well-mixed marine boundary layer (MBL) under a marked temperature inversion maintained by large-scale subsidence. The subtropical MBL and stratocumulus has been the focus of many recent studies, but mid-latitude systems can exert a strong influence. However, this connection is not well established due to debatable model results and few in situ measurements south of 20°S. During a 2-week field campaign in August 2011 at Robinson Crusoe Island (~700 km offshore at 33.6°S), radiosondes were launched to observe the response of the MBL to mid-latitude synoptic forcing. During the observation period a broad, slow-moving cutoff low (COL) passed over the region. Other observations include COSMIC GPS, infrared satellite imagery, TRMM radar reflectivity, and operational radiosondes from the Chilean weather service. A numerical simulation is included to diagnose the synoptic features. The inversion prior to the COL was maintained and lifted above 5 km as the COL passed over the island. Soon after the COL center passed the island, the MBL top did not descend or reform near the surface and then deepen, but rather an inversion reformed at ~2.7 km. Using a variety of datasets, the height of the reformation of the inversion is related to the cloud top height of the scattered shallow cumulus convection under the COL, which coincides with the level of maximum convergence of the vertical velocity.

Responsible editor: J.-F. Miao.

D. A. Rahn (✉)
Atmospheric Science Program, Department of Geography, University of Kansas, 1475 Jayhawk Blvd., 201 Lindley Hall, Lawrence, KS 66045-7613, USA
e-mail: darahn@ku.edu

1 Introduction

Circulation over the southeast Pacific (SEP) is regularly dominated by a surface anticyclone since it is under the subsiding branch of the Hadley circulation. The downward motion maintains a temperature inversion that separates the dry, warm troposphere from the humid, cool marine boundary layer (MBL). The MBL is influenced by a large range of scales from microscale forcing (e.g., entrainment, aerosol–cloud interactions) to the global circulation which ultimately maintains the subsidence inversion (e.g., the Hadley cell). Height of the MBL tends to increase offshore from South America (e.g., Garreaud et al. 2001; Rahn and Garreaud 2010a; Xie et al. 2012) and is often capped by one of the most extensive stratocumulus (Sc) cloud decks in the world (Klein and Hartmann 1993). Properties of Sc are related to MBL depth (Zuidema et al. 2009) and play an important role in the global radiation balance since low-level cloud cover has a net cooling effect. However, representing Sc in global climate models is not trivial (Mechoso et al. 1995; Ma et al. 1996).

Recently, much effort has been put forth to understand the individual components of this system through process studies. One important issue that received much attention is the transition of Sc from the subtropics into trade wind cumulus in the tropics (Wyant et al. 1997; Sandu and Stevens 2011; Xiao et al. 2011). Another transition region is from the mid-latitudes into the subtropics, but it has not been studied extensively. Synoptic systems can have a profound impact on the characteristics of the MBL in the subtropics (Rahn and Garreaud 2010b). Changes under strong synoptic forcing can be large and cause substantial variations to MBL height. For example, the observed range was 750–2,000 m at 80°W, 20°S during VOCALS-REx in austral spring. There is a large annual variation in the

characteristics of the synoptic patterns over the SEP associated with the seasonal march of the storm tracks. Synoptic disturbances over the SEP include baroclinic cyclones and slow-moving barotropic cutoff lows. While the connection between the mid-latitude weather systems and the subtropical MBL has been recognized, details of this connection are sparse and supporting observations are even rarer.

Synoptic influence on boundary layers within a baroclinic system was shown by Sinclair et al. (2010). They used a numerical model that represented an idealized, dry, baroclinic weather system and determined that the characteristics of the synoptically driven boundary layer are driven primarily by the thermal advection. Post-frontal continental Sc in the planetary boundary layer was observed and modeled by Mechem et al. (2010a, b). Behind the surface cold front, the Sc occurred during cold-air and dry-air advection. The temperature inversion was maintained by a shallow layer of ascent near the surface under a deep layer of descent aloft. Turbulence was weak compared to marine Sc, but like marine Sc, the turbulence was generated by longwave radiative cooling at cloud top. Field and Wood (2007) used satellite data to construct composites of the mean fields and probability density functions of various parameters including cloud cover and cloud type associated with mid-latitude cyclones over four oceanic regions.

Painemal et al. (2010) reported results from satellite data, a laser ceilometer, an automatic weather station, and human synoptic reports from January to June of 2003 on San Felix Island (26.3°S, 80.1°W), which is far offshore in the SEP and located near the southern edge of the climatological marine stratocumulus cloud regime. Variability of the low-cloud deck was analyzed alongside daily synoptic maps and indicated that a strong anticyclone typically had large closed cells while the subsidence imposed by mid-latitude wave activity typically had small closed cells. Strong and short-lived significant weather disturbances have a strong impact on the cloud category since the mid-latitude features tend to intrude equatorward into the subtropical stratocumulus region. Cloud type was also speculated to be associated with seasonal differences in the sea surface temperature. Warmer sea surface temperatures during the summer that drive rising thermals are more important in sustaining the large closed cells since the large closed cells are more decoupled than the small closed cells.

The case study presented here demonstrates how the MBL (particularly the temperature inversion associated with the MBL height) changes under fairly strong synoptic forcing originating in the mid-latitudes and its connection to the MBL height into the subtropical latitudes. Because numerical models have provided debatable results, especially when it comes to MBL height (e.g., Wyant et al. 2009), and in situ observations of the lower atmosphere over the SEP are extremely limited, a 2-week field campaign collected observations 700 km offshore of the continent at 33.6°S. Radiosondes were launched twice daily from 30 July to 13 August 2011 (austral winter) to capture at least one synoptic event that disrupts the typical anticyclone over the SEP. The main goal was to measure changes of the MBL in situ to provide a data set that can be used in conjunction with other sources of data (e.g., satellite) to identify key features, which could also be used to assess numerical simulations. During the observing period an approximately barotropic cutoff low (COL) passed slowly over the observation site and drove considerable changes to the MBL in a broad region of the SEP, which is a common occurrence. In fact, the formation of COLs is favored off the Chilean coast (Fuenzalida et al. 2005; Reboita et al. 2010). Due to their common appearance over the region, it is believed that this case study may be used to represent features of other COLs.

Characteristics and changes of the MBL under the COL for this case and its influence that extends farther north are examined. While somewhat descriptive, this case study quantifies several aspects of the MBL response under a COL originating in mid-latitudes, and whose influence can extend well into the subtropics. Section 2 describes the datasets that are used. The results are given in Sect. 3 and are summarized in Sect. 4, which comments on further lines of investigation motivated by some of these findings.

2 Datasets

Few in situ observations are available over the SEP. Operational radiosondes are limited to three sites along the Chilean coast spanning ~2,000 km: Antofagasta (23°S), Santo Domingo (33°S), and Puerto Montt (41°S). In the last decade, several dedicated cruises have been conducted to obtain radiosonde observations over the SEP. These include CIMAR-V (Garreaud et al. 2001) that had a leg along 27°S, and various other cruises along 20°S during the spring from 2001 to 2007 (de Szoeke et al. 2010) and a large international field campaign in austral spring of 2008 (Wood et al. 2011). Additional soundings in central Chile were obtained a year later in 2009 at Lengua de Vaca (30°S) during VOCALS-CUpEx (Garreaud et al. 2011) near a wind maximum that is able to transport aerosols to the northwest (Chand et al. 2010; Allen et al. 2011; Rutllant et al. 2013). As part of a small field campaign in 2011 meant to document the MBL offshore, but farther south of all these cruises, radiosondes were launched from Robinson Crusoe Island (RCI) located at 33.6°S 78.8°W in the Juan Fernandez Archipelago, which is ~700 km west of the continent (Fig. 1). The radiosondes used were the iMet-

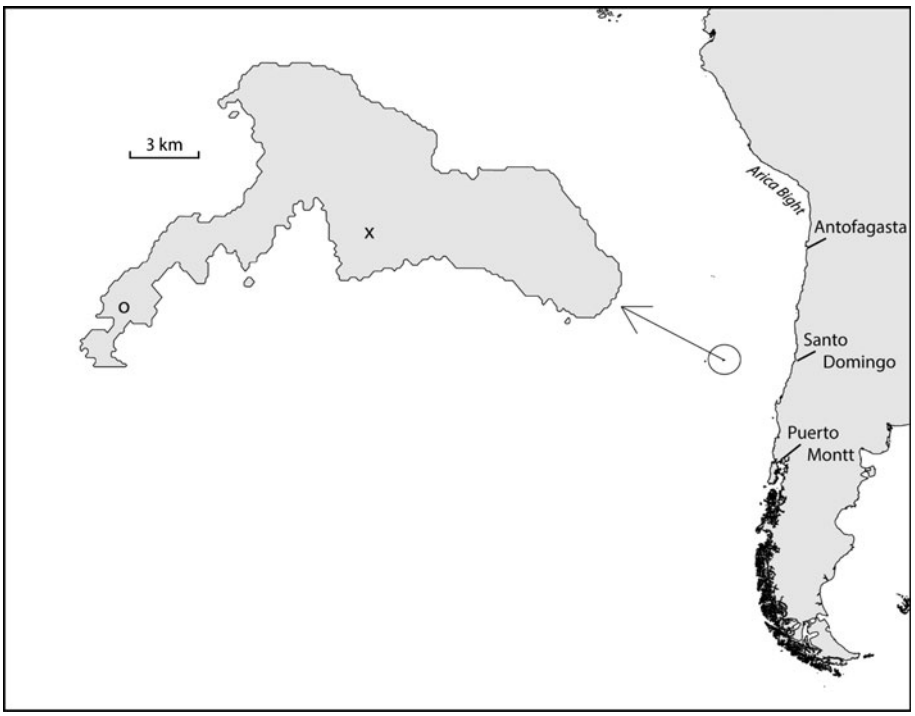

Fig. 1 Location of RCI is indicated by *circle*. The *inset* map of RCI includes the launch site (*circle*) and the highest point on the island (*cross*)

AB from International Met Systems. Because the island's topography could impact the measurements, considerable efforts were made to avoid the highest topography of the island. The radiosondes were launched from the aerodrome on the far southwestern part of the island where there is the lowest elevation and away from the 915 m peak of the island in its center (Fig. 1). To conform to the operational radiosondes, launches occurred twice daily at 00 and 12 UTC starting at 12 UTC 30 July 2011 and ending on 12 UTC 13 August 2011.

A radio occultation (RO) technique utilizing low-earth orbiting satellites and the global positioning system (GPS) is used to infer the height of the MBL and comes from COSMIC GPS (Anthes et al. 2008). The refractivity of the lower atmosphere is primarily a function of water vapor and temperature. A sharp gradient in those quantities, which is the case at the top of the MBL, produces a sharp change in the refractivity. Thus, the MBL height can be remotely sensed and used to augment the number of in situ observations. There are different methods that are typically used to objectively identify the height of the MBL using GPS RO. Two such methods are the break point method (Guo et al. 2011) and the maximum refractivity gradient method (Xie et al. 2012). The breakpoint method is used here. Since there are few GPS RO soundings for the period in total, each sounding in the area during the COL was visually inspected to ensure its quality.

Additional satellite observations come from the geostationary orbiting earth system (GOES) and the tropical rainfall measurement system (TRMM) satellites. Data were obtained from the comprehensive large array-data stewardship system website (http://class.noaa.gov). Brightness temperature is calculated from the channel 4 GOES Imager that has a 10.7 μm central wavelength and a 4 km spatial resolution at nadir. The TRMM precipitation radar operates at 13.8 GHz, cannot detect light or moderate drizzle, and has a spatial resolution of 4.3 km and a vertical resolution of ~250 m at nadir (Kummerow et al. 1998).

Table 1 WRF parameterizations

Parameterization	Scheme	References
Microphysics	Thompson	Thompson et al. (2008)
Longwave	RRTMG	Iacono et al. (2008)
Shortwave		
Land surface	Pleim-Xiu	Xiu and Pleim (2001), Pleim and Xiu (2003)
Surface layer	Pleim-Xiu	Pleim (2006)
PBL	UW	Bretherton and Park (2009)
Cumulus	BMJ	Janjic (1994, 2000)

To simulate the environment during the COL, the weather research and forecasting (WRF) model (Skamarock et al. 2008) was run using a single large domain. The horizontal grid spacing is 20 km (225 × 225 points) and there are 84 vertical levels with ~40–60 m resolution under 2 km. The domain covers the area between 13–51°S and 58–104°W. Specific parameterizations are listed in Table 1. The simulation was initialized at 00 UTC 27 July 2011 using data from the global forecast system, which

also provided the boundary conditions during the simulation.

3 Results

3.1 Synoptic features

West of the South American continent is a zone that favors the development of COLs (Fuenzalida et al. 2005; Reboita et al. 2010). The synoptic characteristics of COLs have been studied fairly extensively in case studies (e.g., Matsumoto et al. 1982; Hill and Browning 1987; Garreaud and Fuenzalida 2007) and in more general studies of upper-level structures (e.g., Palmén and Newton 1969; Keyser and Shapiro 1986). The focus of the following discussion is on one particular event's synoptic features and what occurs under the upper level low near the surface including the corresponding changes to the lower atmosphere with particular attention on the MBL.

A COL had already formed in southern Chile by 28 July 2011 (Fig. 2). The center of the mid-level and quasi-barotropic circulation moves slowly northward over the following 5 days. There is a strong wind to the west and to the north of the center of the upper level low that is a common feature (Garreaud and Fuenzalida 2007). Nearly directly underneath the closed upper level low is a surface cyclone that is near the southern Chile coast, indicating a vertically stacked circulation. Low-level divergence is represented by the column average divergence from 1,000 to 850 hPa that takes place mainly within the MBL. The average was taken to better represent the low-level divergence, which otherwise tends to be a noisy field. Under the COL is low-level convergence which implies a deepening of the MBL. North of the center of the circulation is onshore flow in the lower levels. The onshore flow is effectively blocked by the Andes Cordillera leading to enhanced low-level convergence. As the COL advances northward, the convergence weakens and transitions to divergence so that by 1 August, most of the area is under divergent flow with the exception of the central Chilean coast. Strong divergence also exists on 5 August and extends from central Chile to Peru (not shown). Response of the MBL to these synoptic features is explored in more detail in the next section. However, it is no surprise that the deep MBL begins to thin during the strong low-level divergence.

Compared to the average mid-tropospheric westerly wind and typical migratory systems that both move at ~ 10 m s^{-1}, the COL is a relatively slow-moving feature (Fuenzalida et al. 2005). The relative motion of the wind passing through the COL is important, because air that

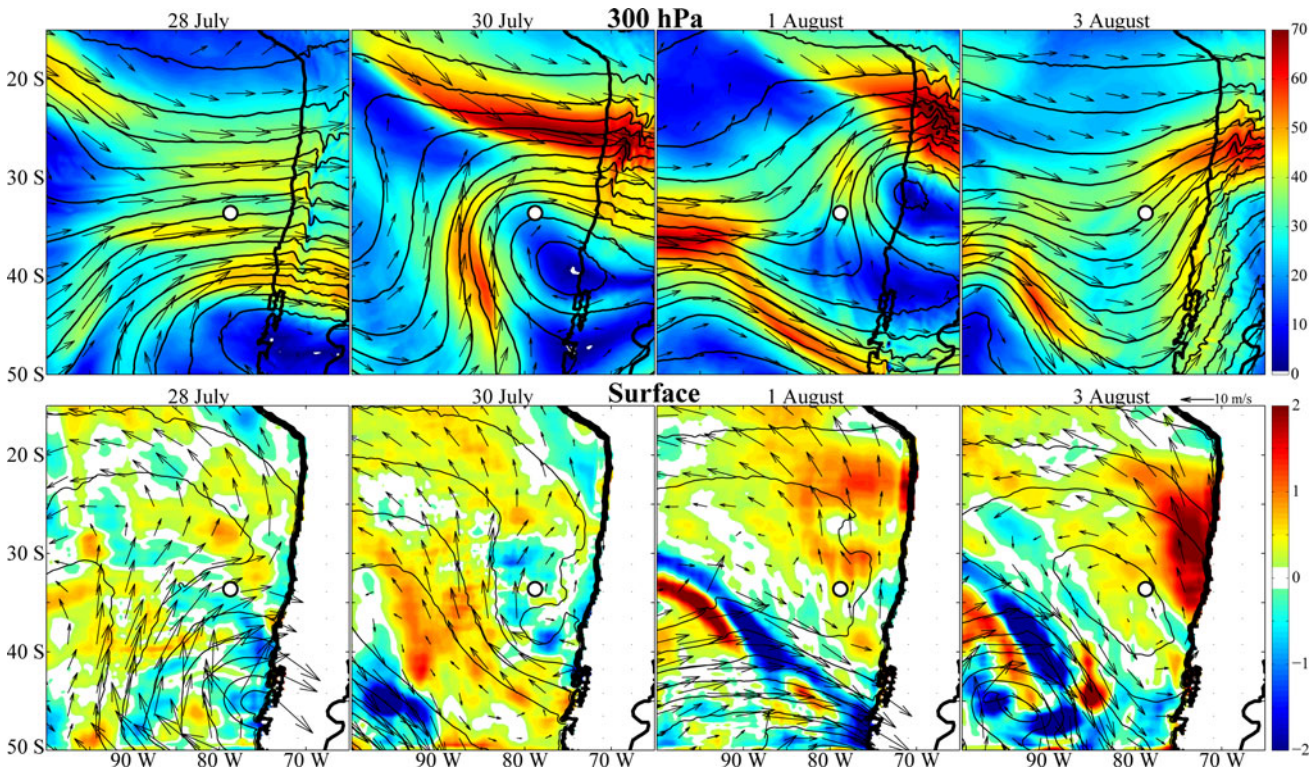

Fig. 2 *Top* the 300 hPa height (m, *contours*), wind speed (m s^{-1}, *color*), and wind vectors. *Bottom* the mean sea level pressure (hPa), column average (1,000–850 hPa) divergence (10^{-5} s^{-1}, *color*) and column average wind vectors. Data from the WRF and the time indicated above each panel. RCI is indicated by the *small circle*. All times are at 00 UTC

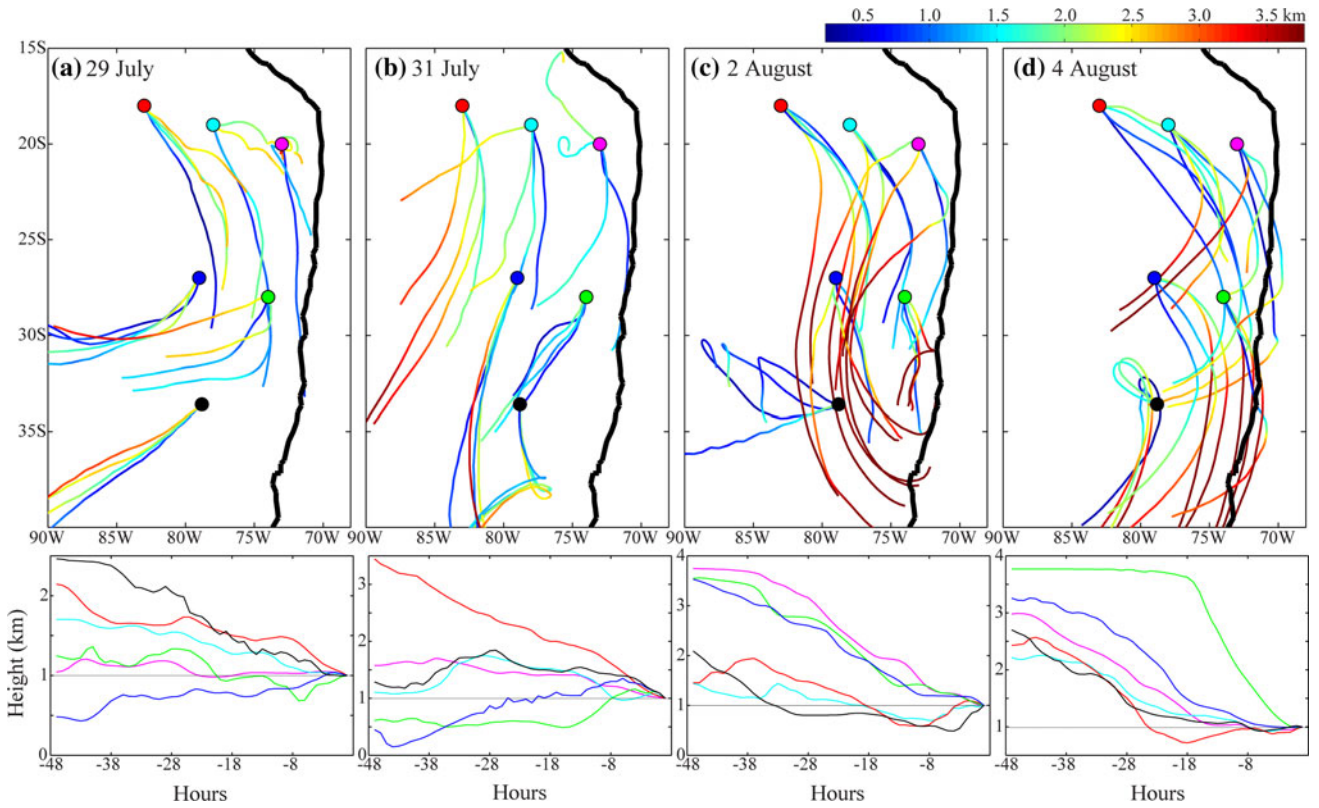

Fig. 3 The 48-h back trajectories from 500, 1,000, 1,500, and 2,000 m at 0000 UTC on **a** 29 July, **b** 31 July, **c** 2 August, and **d** 4 August 2011. *Circles in top panel* are the endpoints and the trajectories are colored according to the height in km (*color scale above*). *Bottom panel* depicts the height over the previous 48 h of the endpoints ending at 1 km, and the *line color* corresponds to the *color of the circles* in the *top panel*. The southern trajectory is RCI

arrives to the subtropics has passed through the mid-latitude system. Back trajectories from 950 hPa along 20°S out to 85°W during a fairly quiescent month are shown by Allen et al. (2011), and it is clear that the air typically originates from the south. During the COL presented here, two-day back trajectories at several locations and heights of 500, 1,000, 1,500, and 2,000 m are calculated from the WRF output using HYSPLIT (Fig. 3). Despite the presence of the large COL, the origin of the air parcels on 29 July in the subtropics is primarily from the south as well. To the south of 25°S on 29 July, the parcels at all levels are arriving from the west or southwest, with some component of the flow moving perpendicular to the coastal topography. This suggests a low-level convergent flow near the central coast that is deflected toward the north by the topography, and is associated with some low-level ascent.

At later times the trajectories indicate that for the most part the air arriving at each particular point has descended after passing through the COL. On 31 July when the COL was at its maximum width and centered over RCI, the low-level trajectories are generally from the south and the southern points tend to show some moderate ascent then descent prior to arriving at the initial location of the back trajectory. On 2 August the back trajectories are generally from the south with cyclonic curvature at upper levels and anticyclonic curvature at lower levels. Rapid descent is also present for the northern points and is no doubt linked to the large low-level divergence that developed on 1 August and strengthened through 3 August (Fig. 2). On 4 August the trajectories are anticyclonic and continue to indicate rapid descent with the sustained low-level divergence. All of these trajectories indicate that the air arriving on the north side of the COL have originated from the south and have descended since 2 August.

3.2 MBL

Underneath the deep cyclonic circulation it is not surprising that the MBL has a strong response to the synoptic conditions. Before proceeding further, a clear definition of the MBL must be stated. The atmospheric boundary layer is typically defined by Stull (1988) as "…that part of the troposphere that is directly influenced by the presence of the earth's surface, and responds to surface forcings with a timescale of about an hour or less." Over the subtropical SEP under normal conditions, the cool, moist, and well-mixed MBL air is contained underneath a prominent temperature inversion that creates an unambiguous top to the

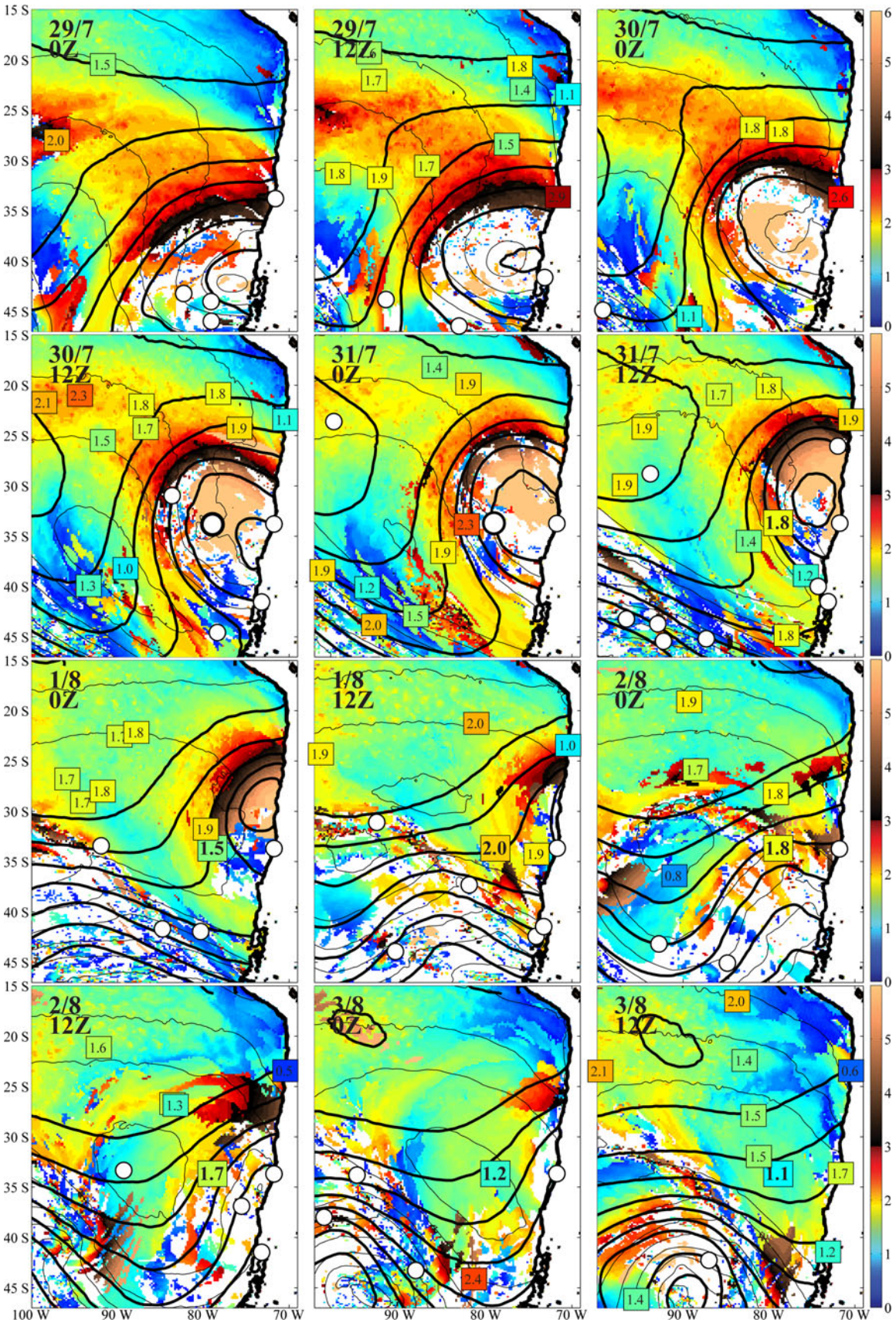
29/7 0Z
29/7 12Z
30/7 0Z
30/7 12Z
31/7 0Z
31/7 12Z
1/8 0Z
1/8 12Z
2/8 0Z
2/8 12Z
3/8 0Z
3/8 12Z
15 S
20 S
25 S
30 S
35 S
40 S
45 S
100 W
90 W
80 W
70 W
0
1
2
3
4
5
6

◀**Fig. 4** Sea level pressure (*thin contours*), 500 hPa height (*bold contours*), and inversion height from WRF (*color scale*, km). Times indicated in the *upper left of each panel*. *Numbers inside boxes* are MBL height from GPS RO or radiosonde measurements and *box color* corresponds to the equivalent in the WRF *color scale*. *Bold numbers* are observations from RCI. The *small white circles* indicate no MBL or ambiguous GPS RO signal. See text for details

boundary layer. It will be shown that the inversion over the SEP, which normally provides an obvious marker for MBL height, can be lifted much higher and change dramatically under conditions such as a COL, as expected. When the temperature inversion is near the surface the height of the temperature inversion base and MBL height are synonymous. When the height of the inversion is much higher, it is not truly associated anymore with the boundary layer (i.e., where the air is directly influenced by the surface). Strictly speaking, this disassociation also happens when a deep MBL is decoupled from the surface (e.g., Jones et al. 2011). In short, not all temperature inversions are associated with the MBL. To define the height of the MBL here in this work, the MBL height is simply the lowest height of the temperature inversion, which is recognized as not necessarily the top of the boundary layer that is directly influenced by the surface, but at least was at one point.

Changes to the synoptic conditions and the MBL as simulated by WRF are illustrated in Fig. 4. This plot includes numbers that represent all of the observations from radiosondes at RCI, Antofagasta, Santo Domingo, and Puerto Montt as well as the inferred MBL height from COSMIC GPS for passes within 6 h of the indicated time. The relatively large time window of the COSMIC GPS increases the number of observations, but at the expense of introducing some discrepancy due to time differences. Color in the box around the numerical MBL height observation corresponds to the model's color scale. A white circle with a black border indicates that there was an observation but no temperature inversion was present or the signal for the GPS RO was too weak or ambiguous. The observations and model are not always in perfect agreement, but for the most part there is consistency between the observational datasets and model solution, contributing credibility to the simulation.

At 00 UTC 29 July the height of the MBL is $\sim$1 km in the Arica Bight. MBL height increases offshore and towards the south, which is a typical structure (Leon et al. 2008; Rahn and Garreaud 2010a; Xie et al. 2012). However, a great increase of the MBL depth toward the south is due to the approaching mid-latitude weather system. In the southernmost part of the domain the COL is already developed and is associated with either no inversion or an inversion height above 6 km (the tropopause). WRF output reveals a substantial gradient in the MBL height from the Arica Bight south toward the center of the circulation. East of 85°W the inversion rises continuously to the south. There are some small discontinuities near the coast, but these likely represent the influence of the nearby coastal topography. Near the center of the circulation the inversion associated with the MBL lifts until it is lost or above 6 km. On 1200 UTC 29 July the MBL is 1.1 km at Antofagasta and 2.9 km at Santo Domingo, which is similar to what the model depicts offshore. This is an extremely large meridional gradient in the MBL height of $\sim$1.6 m km^{-1}. Northwest of the center of the circulation, the MBL height decreases towards the north and northwest. The surface isobars (and wind vectors in Fig. 2) suggest southerly wind just north of the COL center which shifts to southeasterly farther to the north. Thus, the wind is blowing from high MBL height to low MBL height and it can be inferred that there is advection of higher heights north of the COL. Other processes such as changes to the vertical motion are also occurring, but note that the surface wind is generally moving faster than the COL and around this time there is primarily surface convergence in the region (Fig. 2).

The deepest MBL moves northward as the center of the COL migrates slowly northwards and roughly maintains the same height distribution. As the COL moves northward towards the subtropics (for example, on 12 UTC 31 July), on the equatorward side there is a continuous change in the height of the base of the temperature inversion even up to the low tropopause at the center of the COL. This is in contrast to what happens on the poleward side of the COL. Well to the south of the COL the inversion height associated with the MBL increases north towards the center of the COL, but there is a discontinuity with the height of the MBL as it reforms in the lower atmosphere after the COL passes. This so-called "MBL reformation height" after the COL passed was observed between the first RCI radiosonde launch at 1200 UTC 30 July when there was no inversion and 00 UTC 31 July when an inversion reappeared at 2.7 km. The MBL depth becomes shallower on the following days due to subsidence and low-level divergence as inferred from Fig. 2. Descent of the MBL is disrupted by a small shortwave trough that moves through the area around 1–2 August that perturbs the MBL again before the MBL height continues to decrease (<1.5 km) over much of the SEP and becoming much lower on 1200 UTC 3 August.

Features described above are perhaps better represented with a time–height plot located at RCI (Fig. 5). Data are primarily from the simulation, but also included are the observed MBL height and observed potential temperature at two levels (294 and 306 K) indicated by the triangles. The observations generally follow the same trend as the modeled heights. Note that radiosonde launches unfortunately do not start until 1200 UTC 31 June. The inversion height steadily rises after the initial lifting of the MBL until

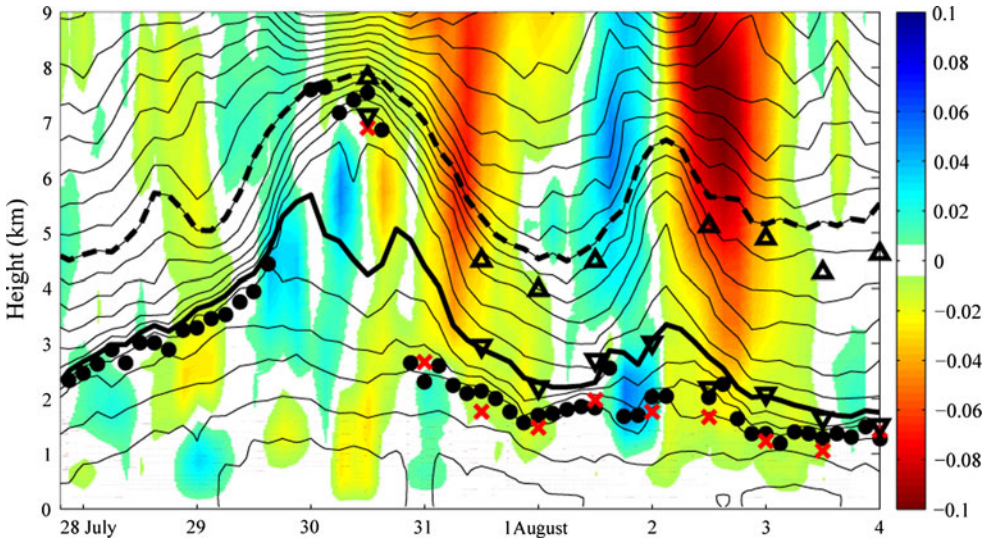

Fig. 5 Time–height graph at 33.6°S, 78.8°W of the model potential temperature (K, *contours*), model vertical motion (m s^{-1}, *color*), model inversion height (*circle*), and sounding inversion height (*red X*). The 294 and 306 K model contour is indicated by *thick*, *solid black contour* and *thick*, *dashed black contour*, respectively. The observed 294 and 306 K height is indicated by *downward and upward pointed triangles*, respectively

reaching a 4 km height on 12 UTC 29 July. Associated with a marked pulse of upward vertical motion over RCI that occurs near the level of the inversion, the temperature inversion that was at one point associated with the MBL is lost until reforming again at 00 UTC 31 July. At 1200 UTC 30 July there is a temperature inversion at ~7 km associated with the low tropopause in the middle of the COL. The MBL inversion north of the COL center was lifted upward and the temperature inversion was maintained well away from the surface until reaching ~4 km. Conversely, a temperature inversion south of the COL center did not subside from above, nor did a temperature inversion reform near the surface and deepen over time. Instead, a temperature inversion reformed near 2.7 km. The initially weak inversion strengthened as it lowered under the increased upper-level subsidence. A strong dipole of vertical motion is present around 00 UTC 2 August and is associated with the mid-level shortwave trough passing over the island. The shortwave interrupted the post-COL decrease of the MBL height. Even though there were large changes in the vertical velocity associated with the shortwave trough, the brief duration prevented a large response in MBL height. Afterwards, the MBL decreased its height once again.

The series of observed and modeled vertical profiles of temperature and dew point are shown in Fig. 6. While there are again differences between the model and observations, the trends are similar. On 12 UTC 30 July the temperature profile is near the moist adiabatic lapse rate from the surface to the tropopause (7 km). Both the observations and also the simulation show a drier layer above ~3 km. This layer becomes even drier over the next 12 h in the observations while not as dry in the model. The observed temperature profile likely contains a measurement error since there is a sharply decreasing temperature after a slight inversion. The height of the small temperature inversion at 00 UTC 31 July also corresponds to a sharp gradient in the measurement of moisture so the height of the MBL is still able to be identified despite the issues with the temperature measurement. The simulation has a weak temperature inversion that just exists between two points and the moisture profile is much wetter than the observations. This makes the defined MBL height of the model less robust than the observations, although it is still identified under the criteria that there is any temperature inversion, however small. After this time the MBL height from the simulation changes greatly every 3 h just after the initial reformation of the MBL height.

In the simulation at 00 UTC 31 July the inversion reforms between weak low-level upward motion and upper-level subsidence (Fig. 5). A time series at RCI of MBL height, surface latent and sensible heat flux, temperature advection, and vertical motion is shown in Fig. 7. Latent heat flux has a peak in the center of the COL. Sensible heat is relatively small, but it is greatest when the center of the COL is over RCI. This is consistent with the coldest air temperatures in the center of the COL (Fig. 5) such that the temperature difference between the surface and air above is the greatest and drives the greatest sensible heat flux. There is weak cold-air advection at 700 hPa (height ~3 km) and 950 hPa (height ~600 m) at the time the MBL reforms at a height of 2.7 km. Just after the reformation of the inversion, the 700 hPa advection

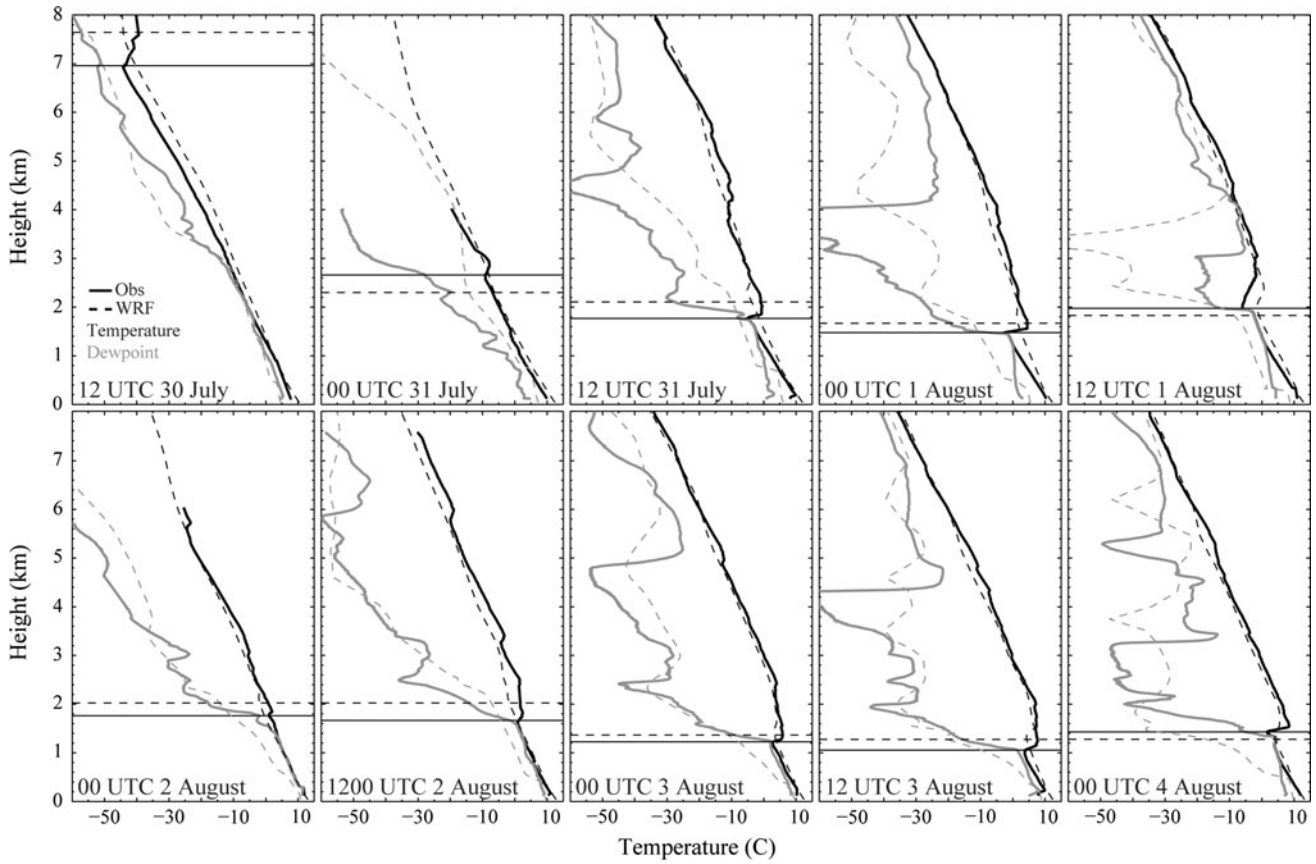

Fig. 6 Observed (*solid*) and simulated (*dashed*) profiles of temperature (*black*) and dew point temperature (*gray*) for the time indicted in each panel. The height of the lowest inversion layer is indicated by the *horizontal line*

becomes 3×10^{-5} K s^{-1} and the 950 hPa temperature advection becomes -5×10^{-5} K s^{-1}. The warm air advection aloft and cold-air advection below strengthens the inversion rapidly after its initial reformation. Vertical motion prior to the reformation of the inversion is upward at 700 hPa and downward at 950 hPa resulting in divergence of the vertical velocities and destabilization above RCI. At the time of the reformation of the inversion the vertical motion is downward at 700 hPa and nearly 0 at 950 hPa. This initial convergence of the vertical velocity strengthens in the hours after the initial reformation when there is upward vertical motion at 950 and the 700 hPa subsidence increases. Large fluctuations of the 700 hPa vertical velocity in August are due to the passage of the shortwave trough. Reformation of the MBL is tied closely to the vertical velocity and after its reformation, strong warm air advection aloft and cold-air advection below reinforce the inversion. Cold-air advection near the surface and a low layer of upward motion under upper-level subsidence is also what was found for a continental Sc case (Mechem et al. 2010a), which in their case was identified as the mechanism that maintains the strong temperature inversion.

In the case presented here, the initial reformation of the inversion appears to be tied to convergence of the vertical velocity as seen at 00 UTC 31 July in Fig. 5. The spatial variability of the height of the maximum vertical velocity convergence under 5 km is found using the WRF output. Since vertical velocity tends to be a noisy field, the horizontal fields were smoothed twice using a discrete convolution with a Gaussian kernel prior to calculating the vertical gradient. The height of the maximum vertical convergence is shown in Fig. 8. The distribution of the heights reflect the position of the COL with higher heights in the middle of the COL. The level of maximum vertical convergence exceeds 3 km in a few locations and much of the COL has values between 2 and 3 km. Even when there is no inversion below 6 km, the level of maximum convergence was between 2 and 3 km. However, the magnitude of the maximum convergence is small where there is no inversion below 6 km. The darkened regions indicate that the stronger vertical convergence is occurring mainly west and south of the COL where the inversion is actually reforming.

The upward motion in the lowest levels weakens over the next 12 h, but the subsidence aloft remains until just

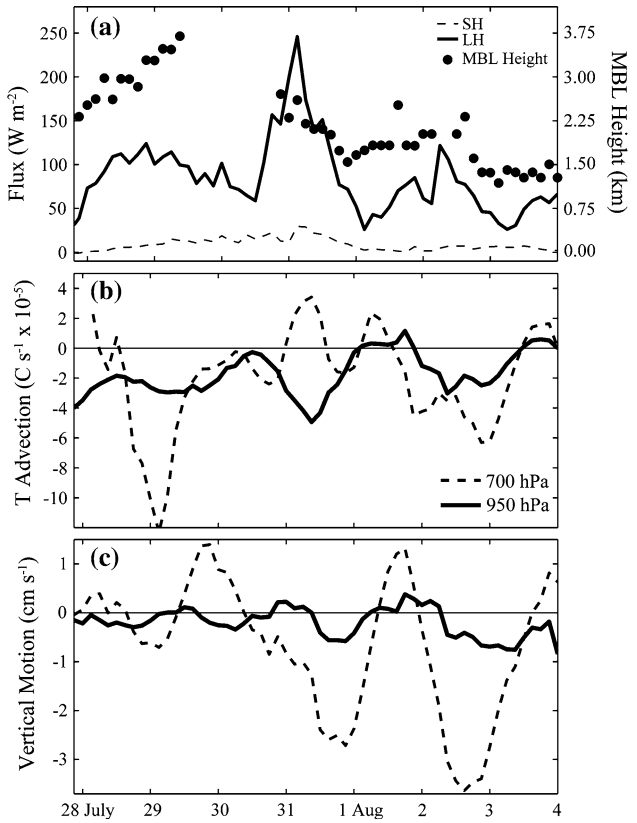

Fig. 7 Time series of WRF output at RCI depicting **a** MBL height (km, *circles*), sensible heat flux (W m^{-2}, *dashed line*), and latent heat flux (W m^{-2}, *solid line*), **b** temperature advection (K s^{-1}, $\times 10^{-5}$) at 700 hPa (*dashed*) and 950 hPa (*solid*), and **c** vertical motion (cm s^{-1}) at 700 hPa (*dashed*) and 950 hPa (*solid*)

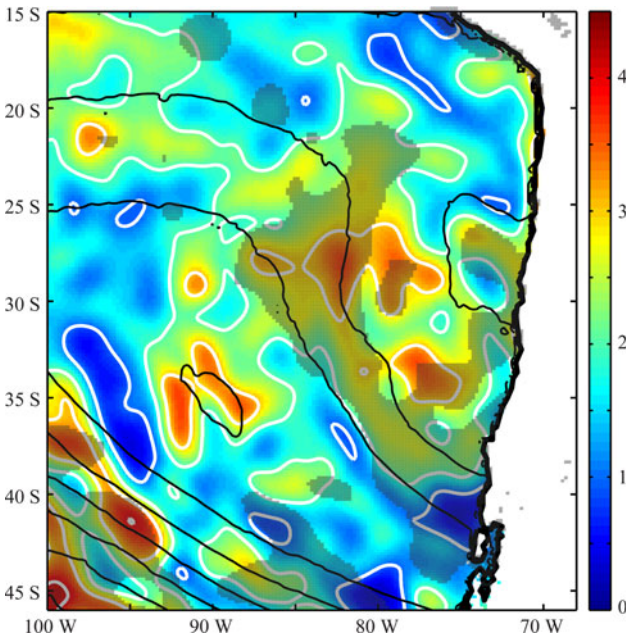

Fig. 8 Altitude (km, *color and white contours* every 1 km) of the maximum convergence of the vertical velocity and sea level pressure (hPa, *black contours*) from WRF at 0000 UTC 31 July 2011. The *darkened regions* are where the magnitude of the vertical convergence is $>2.5 \times 10^{-5}$ s^{-1}

after 00 UTC 1 August. The inversion strengthens and lowers underneath the continued subsidence. The shortwave trough passes over RCI on 12 UTC 1 August and the temperature above the MBL is not correct due to the "wet-bulb effect." The wet-bulb effect is a common problem for radiosonde measurements and happens when the temperature sensor gets wet passing through a cloud and the evaporative cooling after it ascends through the cloud top produces an anomalously cooler temperature. However, it still provides a useful indication of the MBL height, which is the key parameter here. The MBL rose ~600 m due to the passage of the shortwave trough, but resumed decreasing its height to ~1 km on 1200 UTC 3 August.

3.3 MBL cloud

Low-level clouds were predominant during the COL event. Visual observations by the author at RCI revealed scattered to broken low cloud with an occasional tower embedded within the otherwise lower cloud top heights. The embedded tower clouds were not particularly numerous, frequent, deep, or wide but were associated with precipitation. One of these towers even produced small hail as it briefly passed over the launch site at RCI. The first sounding of the 2-week campaign at 12 UTC 30 July sampled the region near the center of the COL (Fig. 9). Here the wind speed exhibited little vertical wind shear, consistent with the straight vertical growth of the towers. There was no temperature inversion until the low tropopause near 7 km, but there was a clear change in the moisture near 3 km. The model output also shows a drying above this level at this time (Fig. 6). Since the model represents a larger area (grid spacing of 20 km), it is reasonable to conclude that this correctly indicates the extent of vertical of mixing from the surface driven by the convection.

Satellite images also suggest that the larger region around the island consisted of the same cloud type as observed at RCI. Figure 10a shows the IR satellite image with the brightness temperatures at 0245 UTC 30 July 2011. This time was chosen because it was roughly between the first radiosonde observation at RCI and the closest TRMM pass at 2200 UTC 29 July shown later. Although the resolution is 5 km, this suggests that there are generally low-clouds with some higher clouds in the region especially around the island under the center of the COL. The distribution of IR-inferred brightness temperatures from each pixel in a large region around the island is given (Fig. 10b). The area of this box is roughly 845 km × 740 km. The west and south portion of the box is extended far away from the island to encompass a large area and capture the lower clouds and the higher clouds

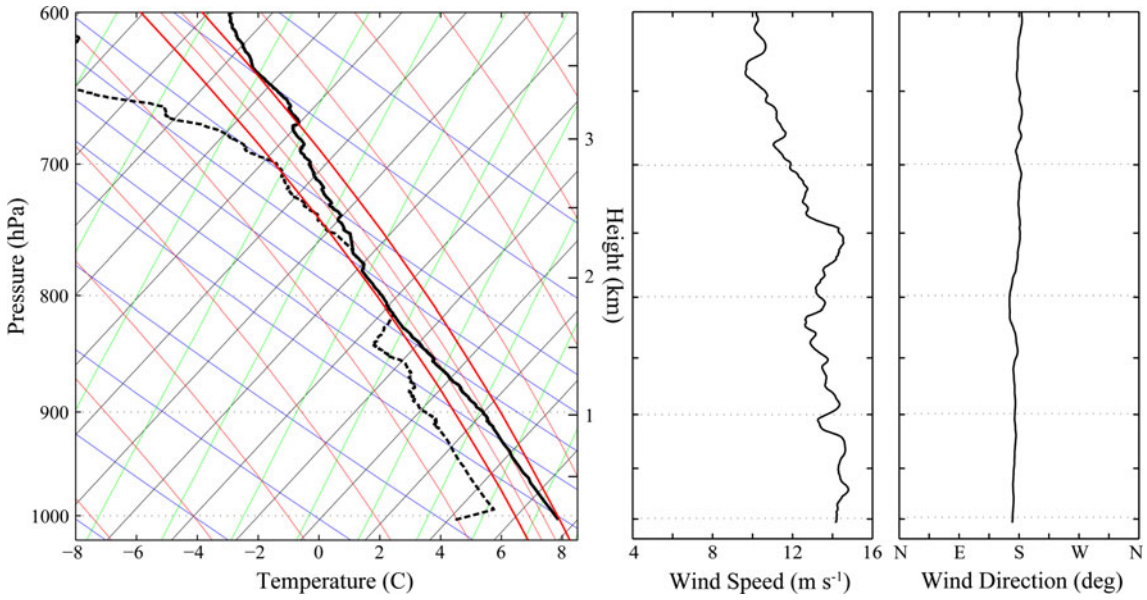

Fig. 9 *Left* Skew-T diagram of the sounding at 12 UTC 30 July 2011 showing the temperature (*solid*) and dew point temperature (*dashed*), *center* the wind speed (m s^{-1}), and *right* the wind direction (°)

associated with the broad COL. The eastern edge of the COL that is near the coastline is often associated with deep convection that is induced by the extra lifting by the topography and is deliberately kept outside the box. While the brightness temperature inferred from the infrared radiance is not the physical temperature, it gives a relative distribution that can be used to infer characteristics of the clouds.

The distribution of brightness temperature consists of three main sections. Because the pixels are 5 km wide, there is an averaging of the entire area, so clouds are not represented as sharply and defining the sections is subjective. The peak near 8 °C is close to the surface temperature. The surface temperature influences the result for many of the pixels since pixels that are not entirely overcast are included. There is a second section (II) between −2.5 °C and the peak at 8 °C that can be considered the top of the stratocumulus layer. Far fewer pixels are colder than −2.5 °C, but there is a clear tail to −25 °C (III). These are likely pixels that are associated with the cooler tops of the embedded towers near the COL center. It is unlikely that the towers will be of uniform height because they will be in the processes of growing and collapsing, hence this also contributes to the smooth distribution. There are few cold pixels, representing the rarity of the deeper convection. To infer the approximate height of these brightness temperatures, the sounding from 12 UTC 30 July is used as a reference and the corresponding height to the given temperature is indicated on the top *x*-axis in Fig. 10b.

Another source of data that reveals the vertical structure of the lower atmosphere comes from a TRMM pass that occurred at 22 UTC 29 July 2011 (Fig. 11). Precipitation rate derived from TRMM reflectivity is overlaid on the IR image and indicates scattered precipitation over the swath. Scattered precipitation over the area comprises small cells but some are fairly intense. Maximum height of the reflectivity is an indication of the height of the cloud towers since the maximum precipitation height is typically near the cloud top height. A histogram of the maximum reflectivity height within the white dashed box indicates a normal distribution with a median near 3.25 km, which is consistent with the height where both the sounding and the model show a drying of the atmosphere. There are some towers above and below, but the average height that the convection achieves is near the observed and simulated height. This suggests that the scattered convection helps to mix the lower part of the atmosphere, and the mixing likely extends all the way to the surface. There is a small increase of precipitation frequency for maximum precipitation heights at about 1.25 km. While it is not statistically significant, it could be associated with heavy drizzle of the stratocumulus. Furthermore, the frequency of drizzle is probably underestimated since the lower threshold of detectable precipitation is 18 dBZ ($\sim$0.7 mm h^{-1}). There is a clear west-to-east gradient of the highest reflectivity that is associated with the COL structure. Maximum height of the reflectivity is between 80 and 76°W, collocated with the center of the stacked vertical low from the observations and numerical simulation shown in Fig. 4.

Even though the temperature profile varies little up to the tropopause at 7 km, the cloud towers appear to have a preference for a certain height. There are a few factors that limit the growth of an individual convective cell. One factor is the lack of vertical wind shear that is seen in

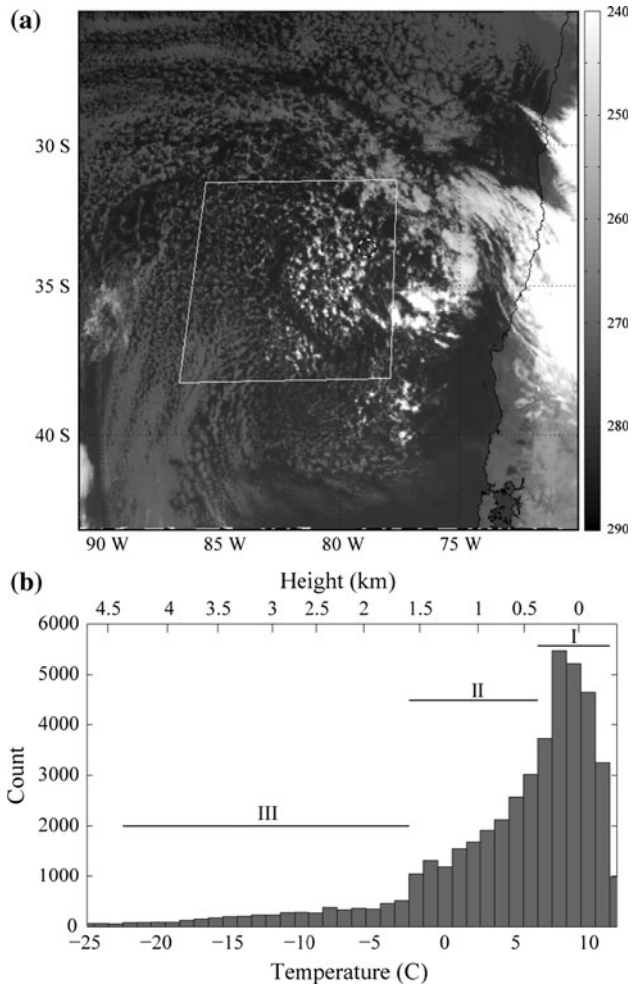

Fig. 10 **a** Brightness temperatures (K, *grayscale*) derived from GOES-13 Channel 4 at 0245 UTC 30 July 2011. RCI is indicated by the *black* and *white circle*. **b** Distribution of brightness temperatures within the *white box* in **a**. Height (km) is approximated by the temperature from the radiosonde launched at 12 UTC 30 July

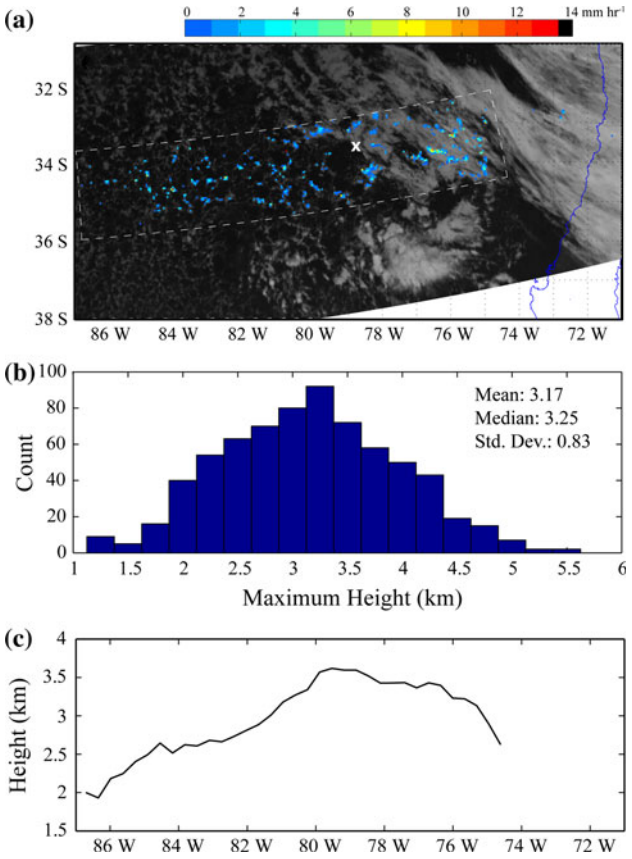

Fig. 11 **a** Brightness temperatures derived from TRMM Channel 4 at 2200 UTC 29 July 2011 and rain rate (mm h^{-1}). RCI indicated by *white X*. **b** Distribution of the maximum height (km) of reflectivity for each column sampled within the *white dashed box*. **c** Meridionally averaged height (km) of the maximum height of reflectivity

Fig. 9. Without vertical wind shear to tilt the updraft and create a sustainable circulation, the growth is inhibited because the downdraft eventually interacts with the updraft, effectively shutting off the convection. Little shear occurs in a barotropic COL. Another limiting factor is the ambient stability, which is set up by the synoptic conditions and modified in turn by the redistribution of heat in the lower atmosphere from the shallow convection. A broad area of shallow, precipitating convection can redistribute heat through latent heat release as the water vapor condenses aloft that warms the upper levels and also through precipitation that falls below the cloud base into the subsaturated air where the evaporative cooling can act to cool the lower levels. These two factors would act to stabilize the lower atmosphere within the generally less stable center of the COL. The observations and simulation of the lower atmosphere including the MBL height in addition to the satellite-derived cloud features shown here do suggest that even though there is no clear temperature inversion or otherwise stable layer that inhibits growth, the cloud top height indicates the extent of mixing in the lower atmosphere and to some extent the influence of the surface. When the more typical MBL reforms, it is noticeably tied to the height of the cumulus towers. The initial reformation of the MBL certainly has implication on the height of the MBL well into the subtropics.

3.4 Implications for subtropics

When the COL is still in the south at 00 UTC 29 July (Fig. 4), the simulated MBL height in the Arica Bight is near 1 km and is slightly deeper towards the west. A GPS occultation at 20°S 90°W indicates a MBL height of 1.5 km that is consistent with model results. At 12 UTC 29 July the sounding at Antofagasta reveals an MBL height of 1.1 km. Just offshore of Antofagasta at about 76°W are two GPS RO that reveal inversion heights of 1.4 and 1.8 km. The model indicates a higher MBL height offshore of Antofagasta that increases rapidly towards the south. The rapid increase in MBL height off the subtropical coast is no doubt related to the COL.

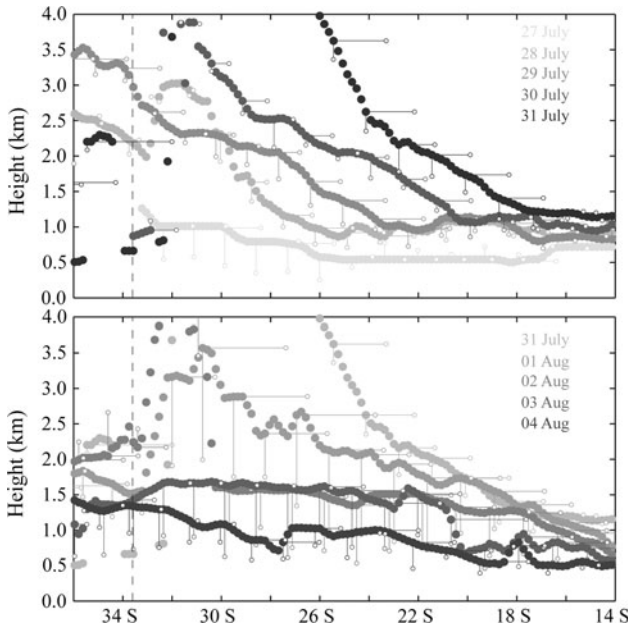

Fig. 12 Meridional cross section of MBL height (m) along 79°W. *Vertical* and *horizontal lines* indicate relative magnitude of the vertical velocity at MBL top and meridional flow, respectively. Times are indicated by the *grayscale in the upper right of each panel*. The *dashed vertical line* indicates the latitude of RCI

Figure 12 depicts the time series of the meridional MBL height from the model along 79°W and includes the meridional wind and vertical motion at the inversion level represented by the horizontal and vertical lines, respectively. The meridional wind and vertical velocity at MBL height indicates that the wind is southerly and there is subsidence near the MBL top. As the COL progresses northward from 27 to 31 July, the MBL clearly deepens while the subsidence at MBL top weakens, but is still present. The MBL deepens most dramatically towards the south while near the coast of Peru at 14°S the MBL deepens about 500 m. As the COL weakens and crosses over the Andes, the perturbed, deep MBL begins to decrease its height. On 1 August the MBL decreases its height in the north, and further towards the south the MBL reforms between 2 and 3 km. The shortwave trough from 2 to 3 August temporarily impedes the lowering of the MBL top, but by 4 August the height is near where it began on 27 July. As expected, the largest changes of the MBL depth are in the south, but the primarily mid-latitude forcing extends towards the subtropics and is associated with an MBL deeper than the mean state.

4 Summary

While much work has been done to understand the transition of the MBL from the subtropics to the tropics, less attention has been given to the connection between the mid-latitudes and subtropics. Part of the challenge is the lack of in situ observations over the SEP to characterize the lower atmosphere, especially within mid-latitude weather systems. While only consisting of 2 weeks of twice daily radiosonde launches, the observations are used in conjunction with other sources such as COSMIC GPS, remote sensing of infrared radiation and precipitation from satellite, and a numerical simulation to characterize the lower atmosphere during a broad, slow-moving COL. A consistency amongst the observational datasets is shown, and these measurements compare well to the numerical simulation. Thus, at least for this case, the large changes to the MBL and in general the lower atmosphere during a COL are adequately modeled. This suggests that using these data sources and including simulations similar to what was done here for many COL events may be used to quantify variability of the MBL including the typical magnitude of MBL height change and the equatorward extent of the mid-latitude influence into the subtropics.

For this case, the MBL inversion prior to the COL arrival is lifted up toward the tropopause as the COL migrates northward. After the COL passes the MBL reforms at $\sim$2.7 km. This altitude is related to the top of the shallow convection that develops underneath the COL, which is not necessarily tied to a temperature inversion but is correlated to the vertical extent of the low-level mixing indicated by the water vapor. Some mixing near the center of the COL is produced by shallow convection, and the vertical growth of the convection is limited by the lack of vertical wind shear. The level of MBL reformation is also associated with the level of maximum vertical convergence and, moreover, where there are relatively high values of the maximum vertical convergence. Hours after the initial reformation the vertical convergence strengthens, and there is cold-air advection below and warm air advection aloft, which acts to strengthen the temperature inversion.

This case study of a COL over the SEP motivates a more comprehensive climatology using the data sources presented in this case study. Particularly, the use of COSMIC GPS and TRMM for many COL events can be aggregated to provide a climatology of the MBL under the effects of mid-latitude synoptic systems and related to reanalysis data, for example. The concurrent modification of the subtropical MBL by these systems could also be linked to quantify the role of mid-latitude forcing on MBL height and cloud properties over the subtropics.

Acknowledgments This project was supported by the Chilean Fondo Nacional de Desarrollo Científico y Tecnológico (FONDECYT) 3110100 and New Faculty Startup funds at KU. Thanks to José Rutllant, Carlos Parra of the Dirección Meteorológica de Chile, and Rosa Zamora for their help during the field campaign on RCI. Roberto Rondanelli helped with processing the satellite data. I also thank two anonymous reviewers for their comments.

References

Allen G, Coe H, Clarke A, Bretherton C, Wood R, Abel SJ, Barrett P, Brown P, George R, Freitag S, McNaughton C, Howell S, Shank L, Kapustin V, Brekhovskikh V, Kleinman L, Lee Y-N, Springston S, Toniazzo T, Krejci R, Fochesatto J, Shaw G, Krecl P, Brooks B, McMeeking G, Bower KN, Williams PI, Crosier J, Crawford I, Connolly P, Allan JD, Covert D, Bandy AR, Russell LM, Trembath J, Bart M, McQuaid JB, Wang J, Chand D (2011) South East Pacific atmospheric composition and variability sampled along 20°S during VOCALS-Rex. Atmos Chem Phys 11:5237–5262. doi:10.5194/acp-11-5237-2011

Anthes RA, Bernhardt PA, Chen Y, Cucurull L, Dymond KF, Ector D, Healy SB, Ho SP, Hunt DC, Kuo YH, Liu H, Manning K, McCormick C, Meehan TK, Randel WJ, Rocken C, Schreiner WS, Sokolovskiy SV, Syndergaard S, Thompson DC, Trenberth KE, Wee TK, Yen NL, Zhang Z (2008) The COSMIC/FORMOSAT-3 mission: early results. Bull Am Meteorol Soc 89:313–333. doi:10.1175/BAMS-89-3-313

Bretherton CS, Park S (2009) A new moist turbulence parameterization in the Community Atmosphere Model. J Clim 22:3422–3448

Chand D, Hegg DA, Wood R, Shaw GE, Wallace D, Covert DS (2010) Source attribution of climatically important aerosol properties measured at Paposo (Chile) during VOCALS. Atmos Chem Phys 10:10789–10801. doi:10.5194/acp-10-10789-2010

de Szoeke SP, Fairall CW, Wolfe DE, Bariteau L, Zuidema P (2010) Surface flux observations on the southeastern tropical Pacific Ocean and attribution of SST errors in coupled ocean–atmosphere models. J Clim 23:4152–4174

Field PR, Wood R (2007) Precipitation and cloud structure in midlatitude cyclones. J Clim 20:233–254

Fuenzalida HA, Sanchez R, Garreaud RD (2005) A climatology of cutoff lows in the Southern Hemisphere. J Geophys Res 110:D18101. doi:10.1029/2005JD005934

Garreaud R, Fuenzalida H (2007) The influence of Andes on cutoff lows: a modeling study. Mon Weather Rev 135:1596–1613

Garreaud RD, Rutllant J, Quintana J, Carrasco J, Minnis P (2001) CIMAR-5: a snapshot of the lower troposphere over the subtropical southeast Pacific. Bull Am Meteorol Soc 82:2193–2207

Garreaud RD, Rutllant JA, Muñoz RC, Rahn DA, Ramos M, Figueroa D (2011) VOCALS-CUpEx: the Chilean upwelling experiment. Atmos Chem Phys 11:2015–2029

Guo P, Kuo Y-H, Sokolovskiy SV, Lenschow DH (2011) Estimating atmospheric boundary layer depth using COSMIC radio occultation data. J Atmos Sci 68(8):1703–1713. doi:10.1175/2011JAS3612.1

Hill EF, Browning KA (1987) Case study of a persistent mesoscale cold pool. Meteorol Mag 116:297–309

Iacono MJ, Delamere JS, Mlawer EJ, Shephard MW, Clough SA, Collins WD (2008) Radiative forcing by long-lived greenhouse gases: calculations with the AER radiative transfer models. J Geophys Res 113:D13103

Janjic ZI (2000) Comments on "Development and evaluation of a convection scheme for use in climate models." J Atmos Sci 57:3686

Janjić ZI (1994) The step-mountain eta coordinate model: further developments of the convection, viscous sublayer and turbulence closure schemes. Mon Weather Rev 122:927–945

Jones CR, Bretherton CS, Leon D (2011) Coupled vs. decoupled boundary layers in VOCALS-Rex. Atmos Chem Phys 11:7143–7153. doi:10.5194/acp-11-7143-2011

Keyser D, Shapiro MA (1986) A review of the structure and dynamics of upper level frontal zones. Mon Weather Rev 114:452–499

Klein SA, Hartmann DL (1993) The seasonal cycle of low stratiform clouds. J Clim 6:1587–1606

Kummerow C, Barnes W, Kozu T, Shiue J, Simpson J (1998) The Tropical Rainfall Measuring Mission (TRMM) sensor package. J Atmos Ocean Technol 15:809–816

Leon DC, Wang Z, Liu D (2008) Climatology of drizzle in marine boundary layer clouds based on 1 year of data from CloudSat and Cloud-Aerosol Lidar and Infrared Pathfinder Satellite Observations (CALIPSO). J Geophys Res 113:D00A14. doi:10.1029/2008JD009835

Ma CC, Mechoso CR, Robertson AW, Arakawa A (1996) Peruvian stratus clouds and the tropical Pacific circulation: a coupled ocean-atmosphere GCM study. J Clim 9:1635–1645

Matsumoto SK, Ninomiya K, Hasegawa R, Miki Y (1982) The structure and role of a subsynoptic cold vortex on the heavy precipitation. J Meteorol Soc Jpn 60:339–353

Mechem DB, Kogan YL, Schultz DM (2010a) Large-eddy observation of post-cold-frontal continental stratocumulus. J Atmos Sci 67:3368–3383. doi:10.1175/2010JAS3389.1

Mechem DB, Kogan YL, Schultz DM (2010b) Large-eddy simulation of post-cold-frontal continental stratocumulus. J Atmos Sci 67:3835–3853. doi:10.1175/2010JAS3467.1

Mechoso CR, Robertson AW, Barth N, Davey MK, Delecluse P, Gent PR, Ineson S, Kirtman B, Latif M, Le Treut H, Nagai T, Neelin JD, Philaner SGH, Polcher J, Schopt PS, Stockdale T, Suarez MJ, Terray L, Thual O, Tribbia JJ (1995) The seasonal cycle over the tropical Pacific in coupled ocean-atmosphere general circulation models. Mon Weather Rev 123:2825–2838

Painemal D, Garreaud R, Ruttlant J, Zuidema P (2010) Southeast Pacific stratocumulus: high-frequency variability and mesoscale structures over San Felix Island. J Appl Meteorol Climatol 49:463–477

Palmén E, Newton CW (1969) Atmospheric circulation systems: their structure and physical interpretation. Academic Press, New York

Pleim JE (2006) A simple, efficient solution of flux–profile relationships in the atmospheric surface layer. J Appl Meteorol Climatol 45:341–347

Pleim JE, Xiu A (2003) Development of a land-surface model. Part II: data assimilation. J Appl Meteorol 42:1811–1822

Rahn DA, Garreaud R (2010a) Marine boundary layer over the subtropical southeast Pacific during VOCALS-REx—part 1: mean structure and diurnal cycle. Atmos Chem Phys 10:4491–4506. doi:10.5194/acp-10-4491-2010

Rahn DA, Garreaud R (2010b) Marine boundary layer over the subtropical southeast Pacific during VOCALS-REx—part 2: synoptic variability. Atmos Chem Phys 10:4507–4519. doi:10.5194/acp-10-4507-2010

Reboita MS, Nieto R, Gimeno L, da Rocha RP, Ambrizzi T, Garreaud R, Krüger LF (2010) Climatological features of cutoff low systems in the Southern Hemisphere. J Geophys Res 115:D17104. doi:10.1029/2009JD013251

Rutllant JA, Muñoz RC, Garreaud RD (2013) Meteorological observations in the Northern Chilean coast during VOCALS-REx. Atmos Chem Phys Discuss 12:22783–22811. doi:10.5194/acpd-12-22783-2012

Sandu I, Stevens B (2011) On the factors modulating the stratocumulus to cumulus transitions. J Atmos Sci 68:1865–1881

Sinclair VA, Belcher SE, Gray SL (2010) Synoptic controls on boundary-layer characteristics. Bound-Lay Meteorol 134:387–409. doi:10.1007/s10546-009-9455-6

Skamarock WC, Klemp JB, Dudhia J, Gill DO, Barker DM, Wang W, Powers JG (2008) A description of the advanced research WRF version 3, NCAR Tech Note, NCAR/TN–475+STR

Stull RB (1988) An introduction to boundary layer meteorology. Kluwer Academic, New York

Thompson G, Field PR, Rasmussen RM, Hall WD (2008) Explicit forecasts of winter precipitation using an improved bulk microphysics scheme. Part II: implementation of a new snow parameterization. Mon Weather Rev 136:5095–5115

Wood R, Mechoso CR, Bretherton CS, Weller RA, Huebert B, Straneo F, Albrecht BA, Coe H, Allen G, Vaughan G, Daum P, Fairall C, Chand D, Gallardo Klenner L, Garreaud R, Grados C, Covert DS, Bates TS, Krejci R, Russell LM, de Szoeke S, Brewer A, Yuter SE, Springston SR, Chaigneau A, Toniazzo T, Minnis P, Palikonda R, Abel SJ, Brown WOJ, Williams S, Fochesatto J, Brioude J, Bower KN (2011) The VAMOS Ocean-Cloud-Atmosphere-Land Study Regional Experiment (VOCALS-REx): goals, platforms, and field operations. Atmos Chem Phys 11:627–654. doi:10.5194/acp-11-627-2011

Wyant MC, Bretherton CS, Rand HA, Stevens DE (1997) Numerical simulations and a conceptual model of the stratocumulus to trade cumulus transition. J Atmos Sci 54:168–192

Wyant MC, Wood R, Bretherton CS, Mechoso CR et al (2009) The PreVOCA experiment: modeling the lower troposphere in the Southeast Pacific. Atmos Chem Phys Discuss 9:23909–23953

Xiao H, Wu C-M, Mechoso CR (2011) Buoyancy reversal, decoupling and the transition from stratocumulus to shallow cumulus topped marine boundary layers. Clim Dyn 37(5–6):971–984

Xie F, Wu DL, Ao CO, Mannucci AJ, Kursinski ER (2012) Advances and limitations of atmospheric boundary layer observations with GPS occultation over southeast Pacific Ocean. Atmos Chem Phys 12:903–918

Xiu A, Pleim JE (2001) Development of a land surface model. Part I: application in a mesoscale meteorological model. J Appl Meteorol 40:192–209

Zuidema P, Painemal D, de Szoeke S, Fairall C (2009) Stratocumulus cloud-top height estimates and their climatic implications. J Clim 22:4652–4666